

# Collections of Copper Nanocrystals Characterized by Different Sizes and Shapes: Optical Response of These Nanoobjects

C. Salzemann,<sup>†,‡</sup> I. Lisiecki,<sup>‡</sup> A. Brioude,<sup>‡</sup> J. Urban,<sup>†</sup> and M.-P. Pileni<sup>\*,‡</sup>

Fritz-Haber-Institut der MPG, Abteilung AC, 4-6 Faradayweg, D-14195 Berlin, Germany, and Laboratoire L.M.2.N., U.M.R. C.N.R.S. 7070 Université Pierre et Marie Curie (Paris VI), B.P. 52, 4 place Jussieu, F-752 31 Paris Cedex 05, France

Received: April 6, 2004; In Final Form: June 17, 2004

The use of reverse micelles makes it possible to produce copper nanocrystals characterized by various sizes and shapes. By increasing the water content, the average size of the metallic nanocrystals increases from 3 to 13 nm. Structural investigations clearly indicate the formation of pure copper with various crystallographic structures. The absorption spectra of the corresponding colloidal solutions exhibit two plasmon modes in the UV–visible range, around 560 and 640 nm. The progressive emergence of the first mode (Mie's resonance of a perfect sphere) with the increase in the mean particle size is attributed to a mere finite-size effect. The second resonance is explained in terms of nanocrystal shape.

## I. Introduction

Nanomaterials are an important research field, especially because changing their size and shape can modify their properties. The control of copper nanocrystal size was obtained, for the first time, in our laboratory in 1993,<sup>1,2</sup> and no other similar cases have been reported since then. However, a very large number of nanomaterials have been produced by using reverse micelles as microreactors.<sup>3</sup> The majority of copper particles in the first generation synthesized in reverse micelles are spherical. The nanocrystal sizes are controlled by several parameters such as the micellar size, the intermicellar interaction, and the number of copper ions and reducing agents per micelle.<sup>1,2</sup> Thus, metallic particles with diameters varying from 1 to 13 nm are produced. As expected from the extended Mie theory, there is an increase in the 560 nm plasmon band and a decrease in its broadening on increasing the particle size.

For spherical particles, one collective excitation mode is taken into account. However, for particles having various shapes, several plasmon resonance modes appear to be associated with the various orientations of the particle axes. These different oscillation modes can be observed when the particles are randomly dispersed. Hence, the optical properties of particles having various shapes depend on the particle shape, the polarization of light, and the distributions of the particle orientation.<sup>4,5</sup>

In this paper, we demonstrate that spherical reverse micelles induce not only spheres but also other particle shapes. To identify the copper clusters involved in the growth processes of copper nanocrystals, or those formed at the end of the synthesis, the optical properties of such assemblies obtained from experiments are compared to those obtained by simulation using the discrete dipole approximation (DDA) for various clusters with different shapes.

## II. Experimental Section

**Chemicals.** AOT and hydrazine were from Sigma and isooctane from Fluka. The materials were used without further

purification. Copper bis (2-ethylhexyl)sulfosuccinate, Cu(AOT)<sub>2</sub>, was prepared as described previously.<sup>6</sup>

**Apparatus.** Absorption spectra were recorded on a conventional Varian Cary 1 spectrophotometer.

Transmission electron micrographs (TEM) were obtained using a Philips CM200 FEG microscope operating at 200 kV, Cs = 1.35 mm with an information limit better than 0.18 nm. Together with overview images, high-resolution images and electron diffraction patterns were also obtained.

## III. Synthesis of Nanocrystals

Colloidal copper nanocrystals are obtained by mixing two solutions. The first is a mixed micellar solution of copper and sodium AOT ([AOT] = 0.1 M; [Cu(AOT)<sub>2</sub>] = 10<sup>-2</sup> M) in isooctane. The second contains the hydrazine used as the reducing agent. The hydrazine concentration to the Cu(AOT)<sub>2</sub> concentration ratio is 3. The overall water content, defined as  $w = [\text{H}_2\text{O}]/[\text{AOT}]$ , varies from 1.5 to 15. The reaction takes place over 5 h. A few drops of solution are deposited on a copper grid covered by amorphous carbon; then, after total evaporation of the solvent, nanocrystals are observed by TEM. To avoid metal oxidation, the entire procedure is carried out in a glovebox with a nitrogen flow.

## IV. Numeric Optical simulations: Discrete Dipole Approximation, DDA

The DDA is a numerical method in which the object studied is represented as a cubic lattice of  $N$  polarizable point dipoles localized at  $ri$ ,  $i = 1, 2, \dots, N$ , each one characterized by a polarizability  $\alpha_i$ . There is no restriction on the localization of cubic lattice sites so that the DDA represents a particle of arbitrary shape and composition. The object is excited by a monochromatic incident plane wave  $E_{\text{inc}}(r, t) = E_0 e^{ik \cdot r - i\omega t}$ , where  $r$ ,  $t$ ,  $w$ ,  $k = w/c = 2\pi/\lambda$ ,  $c$ , and  $\lambda$  are the position vector, the time, the angular frequency, the wavevector, the speed of light, and the wavelength of the incident light, respectively. Each dipole of the system is subjected to an electric field consisting of two main contributions: the incident radiation field  $E_{\text{inc},i}$  and

<sup>†</sup> Fritz-Haber-Institut der MPG.

<sup>‡</sup> Université Pierre et Marie Curie (Paris VI).

the field radiated by all other induced dipoles  $E_{\text{dip},i}$ . The local field at each dipole is then given by (1).

$$E_{i,\text{loc}} = E_{\text{inc},i} + E_{\text{dip},i} = E_0 e^{ik \cdot r_i} - \sum_{j \neq i} A_{ij} P_j \quad (1)$$

$P_i$  is the dipole moment of the  $i$ th element and  $A_{ij}$  with  $i = j$  is an interaction matrix with  $3 \times 3$  matrixes as elements described by (2).

$$A_{ij} P_j = \frac{e^{ikr_{ij}}}{r_{ij}^3} \left\{ k^2 r_{ij} \times (r_{ij} \times P_j) + \frac{(1 - ikr_{ij})}{r_{ij}^2} [r_{ij}^2 P_j - 3r_{ij}(r_{ij} P_j)] \right\} \quad (2)$$

Once we have solved the  $3N$ -coupled complex linear equations given by relation 3 and determined each dipole moment  $P_i$ , we can find the absorption cross sections for a defined target in terms of the dipole moments as in (4) where \* signifies a complex conjugate.

$$P_i = \alpha_i E_{i,\text{loc}} \quad (3)$$

Note that the metal dielectric constant and that of the surroundings enter into the calculation through a factor  $[\epsilon]/[\epsilon]_0$ , containing the polarizabilities  $\alpha_i$ . In our calculation, the wavevector  $k$  should be multiplied by  $([\epsilon]_0)^{1/2}$  because particles are studied in a diluted solution with a refractive index assumed to be around 1.39. The explicit formula for  $\alpha_i$  was developed by Draine and Goodman.<sup>7</sup>

$$C_{\text{abs}} = \frac{4\pi k}{|E_0|^2} \sum_{i=1}^N \left\{ \text{Im}[P_i (\alpha_i^{-1})^* P_i^*] - \frac{2}{3} k^3 |P_i|^2 \right\} \quad (4)$$

To solve the complex linear equations in DDA, we used the code adapted by Draine and Flatau.<sup>8,9</sup> In actual practice, there are significant advantages associated with performing the sum over dipole fields in eq 1 using the fast Fourier transform methods<sup>10</sup> and in substituting eqs 1 and 2 in 3, we obtain a relation of the form  $A'P = E$  that we can solve with the complex conjugate gradient techniques.  $A'$  is a  $3N \times 3N$  matrix constructed from  $A$  and for a system with a total of  $N$  elements,  $E$  and  $P$  are  $3N$ -dimensional vectors. One of the advantages of this technique is that it allows a certain arbitrariness in the construction of the array of dipole points that represent the studied target in a given geometry. For example, the geometry of the grid where dipoles have to be located is usually chosen to be cubic but it is not uniquely determined. Obviously, the gridding associated with the DDA calculation creates distortion of the particle surfaces, but except for the layer closest to the surface, the fields are smooth and well-converged. In a recent publication,<sup>5</sup> the question of the number of dipoles needed to mimic the continuum macroscopic particle (to approach a homogeneous particle) with an array of discrete dipoles is treated. The answer seems not to be straightforward, because the convergence of physical quantities is related to the number of dipoles.<sup>5</sup> Typically, cross sections calculated with the DDA are accurate to a few percent if  $N \geq 10^4$  dipoles are used. As has been presented previously, we have a matrix of  $(3N)^2$  complex elements which would require a large amount of computational effort.

## V. Results and Discussion

The copper nanocrystals are synthesized in reverse micelles. Because the solution is optically clear, it is possible to obtain

**TABLE 1: Average Diameter of Nanocrystals ( $d$ ), Polydispersity in nm ( $\delta$ ), and the Size Distribution ( $\sigma(\%) = \delta(\text{nm})/d(\text{nm}) \times \sigma(100)$ )**

$w$	1.5	3	4	5	10	15
average size $d$ (nm)	3	5.7	8.4	12	12.8	12.8
polydispersity $\sigma$ (nm)	0.6	0.94	1.8	1.9	1.8	2
polydispersity $\sigma$ (%)	18.3	17.5	20.2	16	14.8	14

simultaneously the optical properties and the TEM images of the produced nanocrystals. Figure 1 shows TEM images of copper nanocrystals at the end of the synthesis (5 h). The patterns correspond to syntheses made at water contents,  $w = [\text{H}_2\text{O}]/[\text{AOT}]$ , varying from 1.5 to 15. The corresponding size histograms presented as insets are made by measuring the diameters of about 500 particles. By increasing the  $w$  value, drastic changes can be observed:

(i) From  $w = 1.5$  to  $w = 10$ , the mean diameter of nanocrystals increases from 2.9 to 12.8 nm, (see histogram insets in figures from Figure 1A to Figure 1E and Table 1). Above  $w = 10$ , the particle size remains unchanged (Figure 1, parts E and F).

(ii) The size distribution (expressed in nanometers,) gradually increases from 0.6 to 2 nm (insets in Figure 1 and Table 1).

(iii) The chemical reduction yield of copper ions increases with  $w$ , inducing an increase in the number of nanocrystals formed. Indeed, at low  $w$ , nanocrystals are relatively sparse on the carbon film while their density increases with increasing  $w$  (Figure 1). This fact is further confirmed by the increase in the 560 nm plasmon peak intensity at high  $w$  when sizes stay almost constant, (see below).

These data are in good agreement with those observed previously.<sup>1</sup> The changes in the particle size and production yield are related to the water structure:<sup>11,12</sup> At very low  $w$  values, the reactants are poorly hydrated and then the yield of the reduction reaction is very low. Such a reaction gives rise to small nanocrystals. Conversely, the increase in the reactant hydration induces the increase in the reaction yield so that the number of nuclei increases. Then, the size distribution and the production of copper nanocrystals increase. By assuming that all the system is totally hydrated at  $w = 15$ , the size, the size distribution, and the production yield of copper nanocrystals should behave similarly up to this critical value. However, this is not the case since copper nanocrystal growth significantly reduces from  $w = 5$  and then stops at  $w = 10$ . This behavior is attributed to the capping with the AOT surfactant molecules. This assumption is supported by the fact that such nanocrystals with a diameter of about 13 nm are larger than the host micelles whose diameter is 6 nm at  $w = 15$ . Under such conditions, the strong nanocrystal–surfactant interactions induce a limiting final nanocrystal size.

A careful observation of the TEM images indicates that at low water content ( $w = 1.5$  and 3) the particles look like spheres (Figure 1, parts A and B) whereas at higher water content, i.e., for larger nanocrystals they present either facets or various shapes (from Figure 1C to Figure 1F). At  $w = 15$  (Figure 1F), the relative percentage of spheres is 66.8%, while cubes, elongated particles, and tetrahedral particles are 8.4%, 7%, and 17.8%, respectively. From simulated optical properties of spherical nanocrystals differing by their sizes (Figure 2) we could expect, according to the TEM images that show mostly spherical nanocrystals, a similar behavior for nanocrystals dispersed in solution (Figure 3). Figure 2 shows a continuous rising absorption below 530 nm due to the interband transitions for very small nanocrystals. As the particle size increases from 3 to 13 nm, the well-known resonance plasmon peak centered

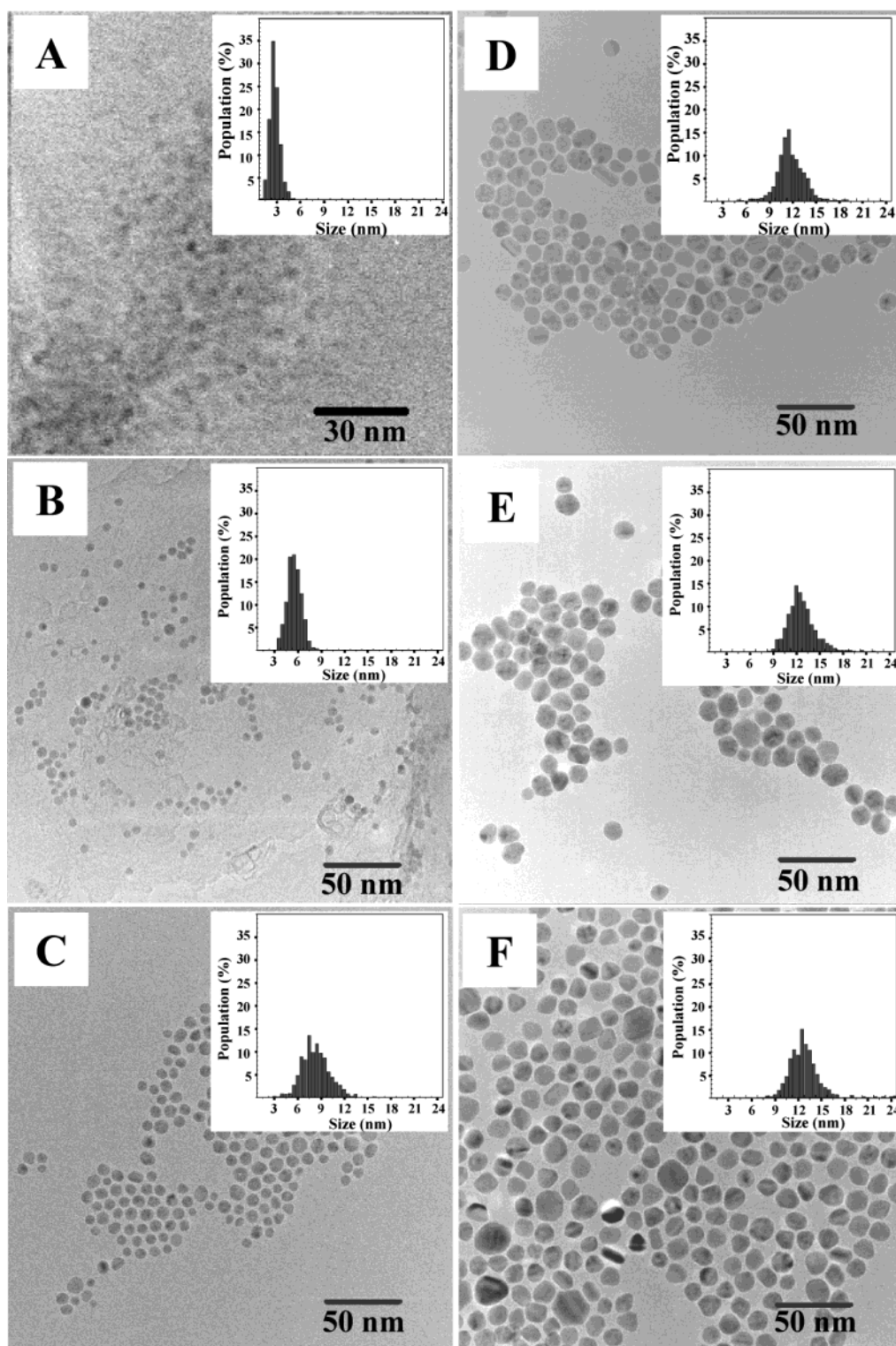


**Figure 1.** Electron microscopy patterns of copper metallic particles synthesized in  $\text{Cu}(\text{AOT})_2/\text{NaAOT}$ , water, isooctane reverse micelles at various water contents.  $[\text{AOT}] = 0.1 \text{ M}$ ;  $[\text{Cu}(\text{AOT})_2] = 10^{-2} \text{ M}$ . Insets (size histograms): (A)  $w = 1.5$ ; (B)  $w = 3$ ; (C)  $w = 4$ ; (D)  $w = 5$ ; (E)  $w = 10$ ; (F)  $w = 15$ .

at 560 nm, corresponding to the dipolar surface plasmon excitation in a metallic sphere, progressively emerges. It is described classically as the collective oscillation of the conduction electron cloud relative to the ionic background. As predicted, the absorption spectrum of 3 nm average size copper nanocrystals, is characterized by a continuous smooth curve (Figure 3A). As the nanocrystal size increases, a noticeable resonance band around 560 nm appears to transform finally into a well-defined peak for samples characterized by a mean

diameter above 4 nm (Figure 3). The intensity of this plasmon peak (560 nm) markedly increases when  $w$  increases from 5 to 15 whereas the average size of nanocrystals remains almost constant (12 nm – 12.8 nm), Table 1. This is due to the increase in the number of particles, i.e., to the increase in the reduction yield. Very surprisingly, a slight increase in the nanocrystal size (from 3 to 6 nm average diameter) induces the appearance of a new resonance around 640 nm (Figure 3A,B). For large nanocrystals this new resonance still exists whereas the TEM



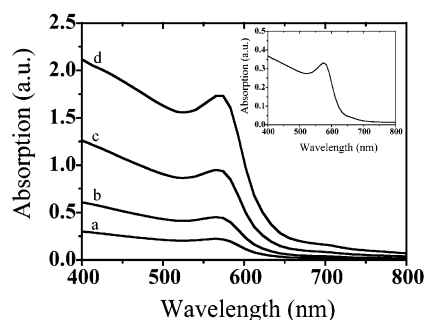


**Figure 2.** Simulation of the optical properties of spherical particles differing by their diameter,  $D$ : (a)  $D = 1.5$  nm; (b)  $D = 3$  nm; (c)  $D = 6$  nm; (d)  $D = 12$  nm. Inset: Simulation of a cuboctahedron particle.

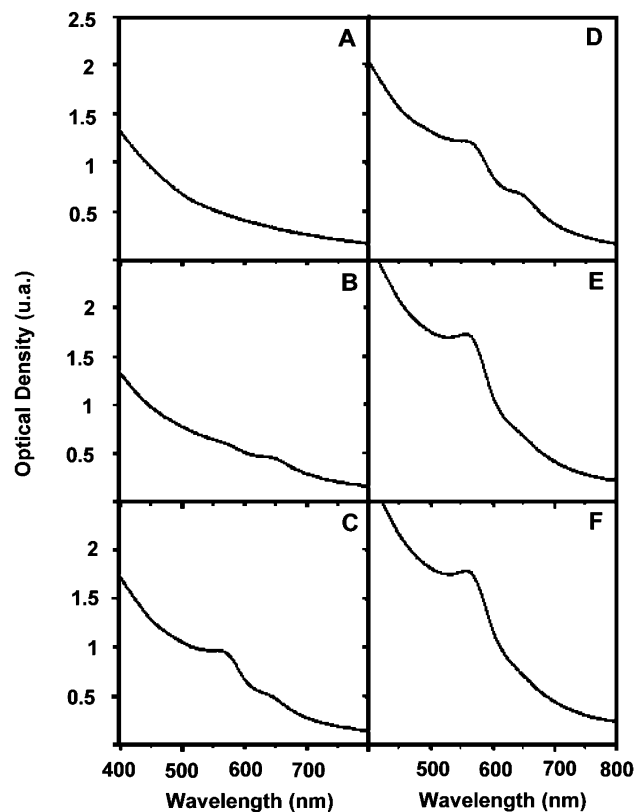


**Figure 3.** Absorption spectra of copper metallic particles synthesized in  $\text{Cu}(\text{AOT})_2/\text{NaAOT}$ , water, isoctane reverse micelles at various water contents.  $[\text{AOT}] = 0.1$  M;  $[\text{Cu}(\text{AOT})_2] = 10^{-2}$  M. Key: (A)  $w = 1.5$ ; (B)  $w = 3$ ; (C)  $w = 4$ ; (D)  $w = 5$ ; (E)  $w = 10$ ; (F)  $w = 15$ .

images show mainly spherical nanocrystals. The intensity of the new resonance (640 nm) remains fairly constant. These experimental and theoretical results confirm that the increase in the spherical nanocrystal size induces the progressive emergence of the 560 nm plasmon resonance. On the other hand, it is well-known that other resonances at lower energies are observed for nanocrystals having a marked change in shape. However, most of copper nanocrystals are spherical. One of the explanations could be due to the fact that the TEM images represent a projection in 2D of a 3D nanocrystal population while the optical properties are related to the particles dispersed in solution. Furthermore, the optical properties are always very sensitive and are able to detect processes which cannot be observed. Simulations using the time-dependent local-density-approximation show rather good agreement with the experimental data by assuming the existence of two populations of nanocrystals composed of 80% spheres and 20% ellipsoidal prolates with an aspect ratio of 2.<sup>14</sup> However, even if TEM

**TABLE 2: Lattice Planes and Reticular Planes of fcc Cu Metal,  $\text{Cu}_2\text{O}$ , and  $\text{CuO}$  and Experimental Reflections**

	(hkl)	$d$ (nm)
copper fcc (Cu)	(111)	0.2087
	(200)	0.1807
	(220)	0.1278
copper oxide cuprite ( $\text{Cu}_2\text{O}$ )	(311)	0.1089
	(111)	0.2465
	(200)	0.2135
	(220)	0.1510
copper oxide tenorite (CuO)	(311)	0.1287
	(002)	0.2530
	(-111)	0.2523
	(111)	0.2323
	(200)	0.2312
experimental reflections	(-202)	0.1866
	(111)	0.210
	(200)	0.182
	(220)	0.130
	(311)	0.110

patterns show the presence of elongated nanocrystals at very high water content (Figure 1F), they are restricted to 7% and no elongated nanocrystals are observed at smaller particle sizes.

Related to the oxidation level of these copper nanocrystals one question arises and two possibilities can be considered:

(i) The particles produced are pure oxide. This is excluded because the electron diffraction patterns show well-defined rings corresponding to the lattice parameters of the fcc structure of pure metallic copper (Table 2). No copper oxide ( $\text{Cu}_2\text{O}$ ,  $\text{CuO}$ ) is detected, otherwise one additional ring (111) should be observed. Moreover, the HRTEM patterns of the nanocrystals (Figure 4) are typically those of the metal derivative.

(ii) The particles are characterized by an oxide shell with a metal core. By considering this assumption, the result has to be related to the thickness of the oxide layer. In the case of a crystalline shell of copper oxide with a thickness higher than 0.5 nm (which corresponds to two lattice planes), lattice planes should be observed by HRTEM (Table 2). For thickness lower than this value, it is quite difficult to determine the presence of oxide surrounding the metal core, even by HRTEM. It has to be noticed that the presence of an amorphous layer of oxide could not be distinguished from the amorphous carbon of the substrate, whatever its thickness. Figure 4 shows white halo surrounding the nanocrystals. These halos cannot be attributed to copper oxide but to the defocus of the microscope. In fact, they result from the optimization of the observation of the lattice planes.

From these structural data, a shell of copper oxide can be excluded.

Nevertheless, these techniques have some limitations to detect a small amount of oxide. We know that the optical responses are very sensitive to surface effects so that, it is more appropriate to detect only few atoms of oxide. In Figure 3, the absorption at 700 nm is quite low whereas according to Yanase et al.<sup>14</sup> the presence of few layers of copper oxide induces a drastic change in the optical properties around 700 nm. From that, it is concluded that if oxide forms at the interface, it is produced in very low proportion compared to the metal core and cannot be detected even by a very sensitive technique as absorption. It is rather difficult to find a technique that could detect such a low amount of oxide. XPS and EDX cannot be used because of the presence of the surfactant containing oxygen in the surrounding. From these data are concluded the formation of the copper metal particles.

In the following, we study, by HRTEM, the structure of nanocrystals produced at various water contents (Figure 4).

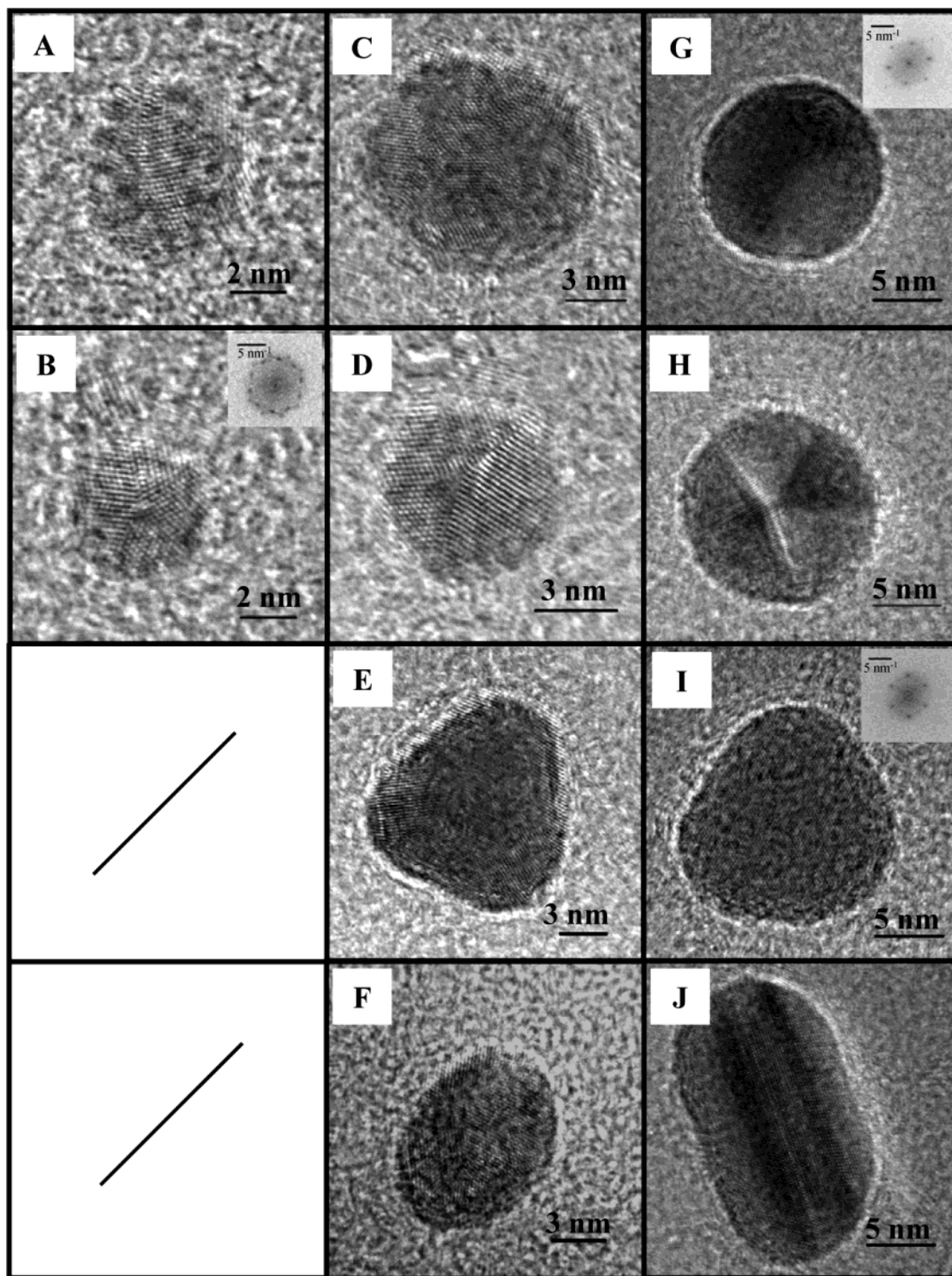


**Figure 4.** HRTEM images of copper nanocrystals synthesized in  $\text{Cu}(\text{AOT})_2/\text{NaAOT}$ , water, isooctane reverse micelles at various water contents.  $[\text{AOT}] = 0.1 \text{ M}$ ;  $[\text{Cu}(\text{AOT})_2] = 10^{-2} \text{ M}$ . Key: (A, B)  $w = 3$ ; (C–F)  $w = 5$ ; (G–J)  $w = 10$ . For images presented in B, G, and I, power spectra are shown in the inset.

Whatever the water content is, the smallest particles are mainly polycrystalline. However some monocrystals are observed. As the size increases with  $w$ , the number of monocrystals increases. Let us list data obtained at various water contents:

(i) At  $w = 3$ , as shown in Figure 4A, there is formation of spherical particles made of fcc clusters. Furthermore, regular decahedra, formed by five deformed tetrahedral subunits and characterized by a 5-fold symmetry, are also obtained (Figure 4B). This is confirmed by the calculated power spectra given in the Figure 4B inset.

(ii) At  $w = 5$ , behavior similar to that obtained at  $w = 3$  is observed with polycrystals made of fcc clusters (Figure 4C) and decahedra (Figure 4D). Furthermore, polycrystal nanoparticles having various shapes such as triangular object (Figure 4E) and ovoids (Figure 4F) are observed.

(iii) At  $w = 10$ , spherical polycrystals are still formed as observed at lower  $w$  values. However the proportion of monocrystals increases. Spherical particles characterized by a regular fcc structure (Figure 4G) coexist with “nearly” spherical particles that are regular decahedra (Figure 4H). Furthermore,

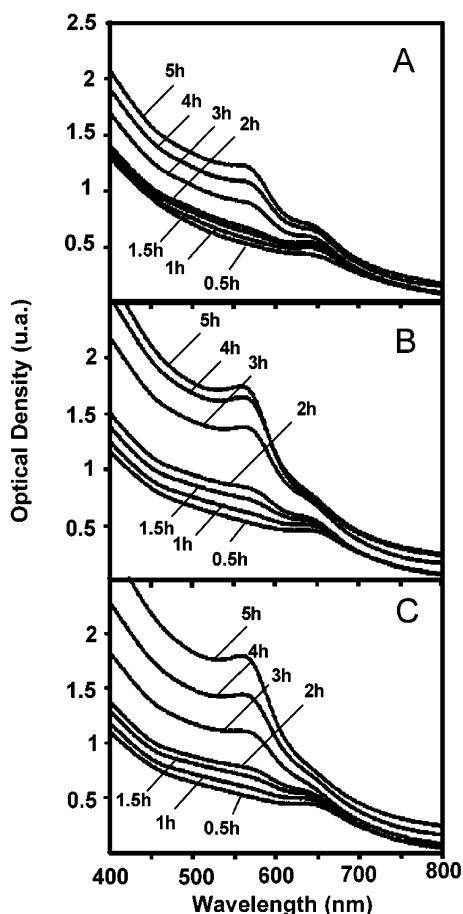


**Figure 5.** Change in the absorption spectrum with time, (from 30 to 300 min) at various water contents  $w = 5$  (A),  $w = 10$  (B), and  $w = 15$  (C).

triangular (Figure 4I) and elongated particles (Figure 4J) are also produced.

The monocrystal spheres and the regular decahedra result from the growth of cuboctahedra and decahedra nuclei, respectively.<sup>15,16</sup> Their shapes are closely related to that of the corresponding nuclei. Conversely, the cylinders and the triangular particles arise from a much more complicated growth process. As concerns the elongated particles, their structure, that has been investigated in previous work,<sup>17,18</sup> is characterized by a truncated large decahedron with 5-fold symmetry. They are the result of additional intermediate (110) planes in a decahedral nucleus. In other words, their formation is induced by the truncation of the five subunit edges of the decahedra nucleus. The initial precursor nucleus evolved in the formation of the triangles, that are also called “trigonal lamellar particles” because of their flatness, is the tetrahedron. In fact, a regular fcc tetrahedron is first truncated on a {111} surface and then twinned by reflection at this surface in such a way that a suitable nucleus for the trigonal lamellar particles can be obtained. Such a bitetrahedral precursor nucleus contains three active sites for growth to maintain the overall 3-fold symmetry in the final nanocrystal.<sup>15,19</sup>

Thus, it clearly appears that all the nanocrystals we produce result from the subsequent growth of three types of nuclei: the cuboctahedron, the decahedron and the tetrahedron.

A kinetic study is performed under various experimental conditions in order to follow the respective behaviors of both resonance bands. Figure 5 shows that at  $w \geq 5$ , the 640 nm resonance band is rapidly formed, i.e., 30 min after the chemical

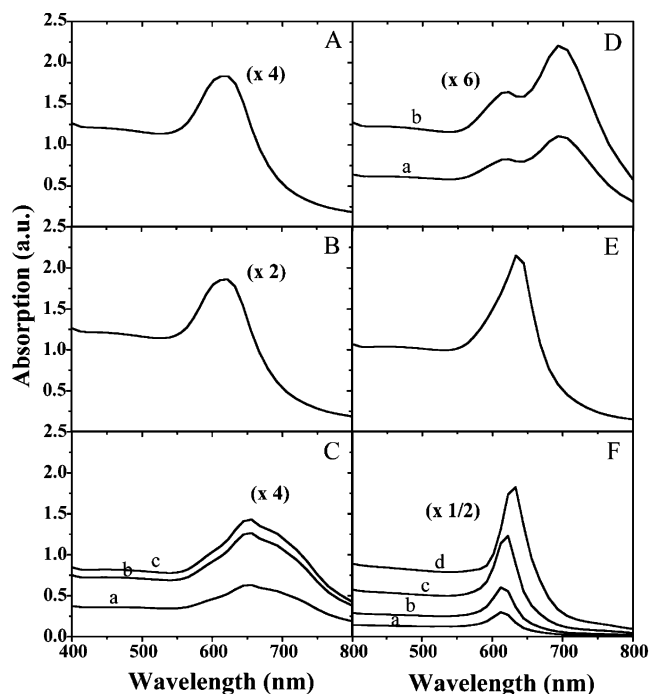


**Figure 6.** Simulated absorption spectra of particles differing by their shapes and sizes: (A) 3 nm decahedron; (B) 6 nm decahedron; (C) (a) 1.5 nm, (b) 3 nm, and (c) 6 nm truncated tetrahedron; (D) (a) 3 nm and (b) 6 nm truncated tetrahedron; (E) 6 nm trigonal prism; (F) (a) 1.5 nm, (b) 3 nm, and (c) 6 nm ellipsoids and (d) 6 nm ellipsoidal particles with an aspect ratio of 2.

reaction starts. The 560 nm resonance band starts to emerge around 1 h later. With time, the two bands behave conversely. Indeed, the 560 nm band becomes dominant compared to that at 640 nm. Finally, at the end of the synthesis, the absorption spectra are characterized by a well-defined peak at 560 nm while a shoulder at around 640 nm is still present. Note that the shoulder becomes less marked when  $w$  increases up to 15, probably because of a diffusion process that tends to hide it. Such a diffusion process originates from the increase of the concentration of nanocrystals. Indeed, the first consequence of this increase is the formation of aggregates in the colloidal solution. The second consequence is probably the increase of the shape polydispersity of nanocrystals. As a matter of fact, the shoulder at 640 nm is less pronounced at  $w = 15$  where the amount of nanocrystals is higher than at  $w = 5$ . Let us remember that the 560 nm peak intensity increases with  $w$  (for any reaction time), which well illustrates the nanocrystal concentration increasing with  $w$ . Nevertheless, the amounts of nanocrystals produced before the end of the synthesis are not high enough; thus, it has not been possible to check by TEM the structures and shapes formed during the kinetic growth.

From these data, the 640 nm resonance band could be due to the formation of seeds involved in the formation of copper nanocrystals (during the first stages of the synthesis) and to anisotropic shape nanocrystals (at the end of the synthesis). The latter should be characterized by either the same shape as the seeds or by a new shape having a similar optical signature. For copper metal materials, the stable precursor nuclei are decahedral, cuboctahedral, and tetrahedral. Let us consider these various copper shapes. The simulated absorption spectrum of 3 nm decahedrons shows a well-defined peak centered at 625 nm (Figure 6A). As the particle size increases from 3 to 6 nm, no change is observed, except that the peak intensity is increased by a factor of 2 (Figure 6B). From HRTEM data, decahedral nanocrystals are observed under the various experimental



conditions, i.e., for various water contents and then various nanocrystal sizes as shown in Figure 4, parts B, D, and H. Hence, from these data, it is reasonable to conclude that the 640 nm resonance band observed a few minutes after the chemical reaction starts is due, at least in part, to decahedral seeds. Now, as for the 640 nm resonance still present at the end of the chemical reaction, it is quite probably due to the presence of decahedral nanocrystals as observed in Figure 4, parts D and H. Note that the slight difference related to the position of the simulated and experimental peaks, i.e., +15 nm, can be due to a slight deformation of the seed. Indeed, it is known that a slight deformation can induce a large change in the spectrum in the low-energy range. This explanation makes sense when the seed involved is a decahedron. Such a multiply twinned particle contains five deformed tetrahedra in order to avoid an angular gap.

At this point, a question arises: Are decahedral precursors and nanocrystals the only shape responsible for the presence of the 640 nm resonance? The simulated absorption spectrum of 6 nm cuboctahedrons is similar to that obtained for spheres with a plasmon resonance centered at 560 nm (inset to Figure 2). This indicates that the 640 nm resonance band cannot be attributed either to seeds or nanocrystals like cuboctahedra. Cuboctahedron-shape nanocrystals are not observed in our experiments, and this is well expected as the growth of such nuclei mostly gives rise to spherical nanocrystals as shown in Figure 4G. Nevertheless, cuboctahedral nuclei are probably present in solution, but their optical signatures cannot be distinct from those of the spheres. Simulations of the optical spectra of tetrahedra differing by their sizes are characterized by an absorption centered at 650 nm and a shoulder at 700 nm. Figure 6C shows similar absorption spectra by varying the particle size from 1.5 to 6 nm. Truncation of 6 nm tetrahedral nanoparticles (implied in the formation of triangles) induces appearance of a peak at 700 nm and a shoulder at 600 nm (Figure 6D). From the position of the resonance peaks shown in Figure 6, parts C and D, it can be concluded that truncated and nontruncated tetrahedra are not responsible for the 640 nm resonance. Nevertheless, they probably are formed but are not concentrated enough to be detected since the corresponding peak intensities are very low (Figure 6C,D).

Now, let us study other shapes different from that of the nuclei: the triangular and the ellipsoidal nanocrystals. The simulated absorption spectrum of 6 nm triangular particles shows a peak centered at 630 nm. As a matter of fact, some triangles are observed for any  $w$  (Figure 4I), and at  $w = 15$ , their relative percentage is 17.8%. Thus, the absorption located at 640 nm could be also due to triangular nanocrystals. Very few (7%) elongated particles are observed. However, the simulation optical spectrum of ellipsoidal particles having an aspect ratio of 2 is characterized by a resonance centered at 630 nm. This other shape could also explain the 640 nm peak. Nevertheless, we have to mention that it is not straightforward to determine the origin of a resonance band (shoulder at 640 nm) with simulations related to well-defined shapes (decahedral, trigonal prism, ellipsoidal) and well-defined sizes. The main purpose that we point out is that this resonance band at 640 nm can be explained as a convolution of closed resonance bands each corresponding to particles of a precise shape and size. However, among the various shapes observed by the microscopy study that we should take into account in this convolution, only the decahedral, the trigonal prism, and ellipsoidal nanocrystals can explain the emergence of this shoulder at 640 nm whatever the size in the range of the distribution.

From these data, it is concluded that immediately after synthesis only the decahedral seeds can be responsible for the high-energy resonance band. Indeed, the cuboctahedral nuclei have an optical signature similar to that of the spheres. The truncated and nontruncated tetrahedra are characterized by a specific absorption that is not detected here. Note that all these three types of nuclei should be formed; otherwise, the various nanocrystal shapes we observed could not exist. As to the decahedral nanocrystals, it is clear that they are mainly responsible for the 640 nm resonance band still visible at the end of the synthesis. In addition, we show that this resonance band can also partly be attributed to the presence of trigonal prisms and ellipsoidal nanocrystals.

## VI. Conclusion

In this paper, we have shown that spherical reverse micelles induce not only spheres but also various other particle shapes like cubes, tetrahedral and ellipsoidal particles. By varying the micellar size, the average diameter of the spherical population can be tuned from 3 to 13 nm. The corresponding absorption spectra show two resonance bands. One is at 560 nm and strongly depends on the copper nanocrystal size. It is related to the plasmon band of spherical copper particles, and the size dependence of the optical properties is in good agreement with simulations using the discrete dipole approximation (DDA). The second resonance band is around 640 nm and does not change with the particle size. From a comparison of the HRTEM and TEM results with the DDA simulations made for various shapes, it clearly appears that this additional resonance band is the signature of the presence of mainly decahedral nanocrystals with ellipsoidal particles and trigonal prisms. In addition, the optical properties indicate the presence of decahedral seeds in the first stages of the chemical reaction.

## References and Notes

- (1) Lisiecki, I.; Pileni, M. P. *J. Am. Chem.* **1993**, *115*, 3887.
- (2) Lisiecki, I.; Pileni, M. P. *J. Phys. Chem.* **1995**, *99*, 5077.
- (3) Pileni, M. P. *Nature Mater.* **2003**, *2*, 145.
- (4) Kelly, K. L.; Coronado, E.; Zhao, L. L.; Schatz, G. C. *J. Phys. Chem. B* **2003**, *107*, 668–677.
- (5) Sosa, I. O.; Noguez, C.; Barrera, R. G. *J. Phys. Chem. B* **2003**, *107*, 6269.
- (6) Petit, C.; Lixon, P.; Pileni, M. P. *Langmuir* **1991**, *7*, 2620.
- (7) Draine, B. T.; Goodman, J. J. *Astrophys. J.* **1993**, *405*, 685.
- (8) Draine, B. T.; Flatau, P. J. Program DDSCAT. University of California, San Diego, Scripps Institute of Oceanography, 8605 La Jolla Fr., La Jolla CA 92093-0221.
- (9) Draine, B. T.; Flatau, P. J. *J. Opt. Soc. Am. A* **1994**, *11*, 1491.
- (10) Goodman, J. J.; Draine, B. T.; Flatau, P. J. *Opt. Lett.* **1991**, *16*, 1198.
- (11) Pileni, M. P.; Hickel, B.; Ferradini, C.; Puchault, J. *Chem. Phys. Lett.* **1982**, *92*, 30.
- (12) Pileni, M. P.; Hickel, B.; Ferradini, C.; Puchault, J. *J. Colloid Interface Sci.* **1983**, *92*, 326.
- (13) Salzemann, C.; Lermé, J.; Urban, J.; Lisiecki, I. Submitted for publication.
- (14) Yanase, *Surf. Sci.* **1991**, *248*, 11.
- (15) Salzemann, C.; Lisiecki, I.; Urban, J.; Pileni, M. P. Submitted for publication.
- (16) Urban, J. *Cryst. Res. Technol.* **1998**, *33*, 7.
- (17) Lisiecki, I.; Filankembo, A.; Sack-Kongehl, H.; Weiss, K.; Pileni, M. P.; Urban, J. *Phys. Rev. B* **2000**, *61*, 4968.
- (18) Lisiecki, I.; Sack-Kongehl, H.; Weiss, K.; Urban, J.; Pileni, M. P. *Langmuir* **2000**, *16*, 8807.
- (19) Kirkland, A. I.; Jefferson, D. A.; Duff, D. G.; Edwards, P. P.; Gameson, I.; Johnson, B. F. G.; Smith, D. J. *Proc. R. Soc. London A* **1993**, *440*, 589.